Narrow line cooling and momentum-space crystals

Thomas H. Loftus,* Tetsuya Ido, Martin M. Boyd, Andrew D. Ludlow, and Jun Ye†

JILA, National Institute of Standards and Technology and University of Colorado, Boulder, Colorado 80309-0440, USA

Narrow line laser cooling is advancing the frontier for experiments ranging from studies of fundamental atomic physics to high precision optical frequency standards. In this paper, we present an extensive description of the systems and techniques necessary to realize 689 nm $^1S_0$-$^3P_1$ narrow line cooling of atomic ^{88}Sr. Narrow line cooling and trapping dynamics are also studied in detail. By controlling the relative size of the power broadened transition linewidth and the single-photon recoil frequency shift, we show that it is possible to smoothly bridge the gap between semiclassical and quantum mechanical cooling. Novel semiclassical cooling processes, some of which explicitly depend on the relative size of gravity and the radiative force, are also explored. Moreover, for laser frequencies tuned above the atomic resonance, we demonstrate momentum-space crystals containing up to 26 well defined lattice points. Gravitationally assisted cooling is also achieved with blue-detuned light. Theoretically, we find the blue detuned dynamics are universal to Doppler limited systems. This paper offers the most comprehensive study of narrow line laser cooling to date.

I. INTRODUCTION

Narrow line magneto-optical traps (MOTs) are rapidly becoming powerful tools in a diverse array of experimental studies. These unique and versatile systems have, for example, already been used as integral components in obtaining fully maximized MOT phase-space densities [1], nuclear-spin based sub-Doppler cooling [2,3], all-optical quantum degenerate gases [4], and recoil-free spectroscopy of both dipole allowed [5] and doubly-forbidden [6] optical transitions. In the future, narrow line MOTs promise to revolutionize the next generation of high precision optical frequency standards [7–9]. Narrow line cooling, via the relative size of the transition natural width Γ and the single-photon recoil frequency shift ω_R, also displays a unique set of thermal-mechanical laser cooling dynamics. In a previous paper [10], we explored these behaviors by cooling ^{88}Sr on the $^1S_0$-$^3P_1$ intercombination transition. In the present work, we significantly expand upon this discussion and provide a comprehensive description of the experimental techniques used to realize and study $^1S_0$-$^3P_1$ cooling and trapping.

Fully understanding narrow line laser cooling requires first clarifying the difference between broad and narrow Doppler cooling lines. Broad lines, historically used for nearly every laser cooling experiment [11], are defined by $\Gamma/\omega_R \gg 1$. The 461 nm ^{88}Sr $^1S_0$-$^1P_1$ transition shown in Fig. 1(a), which typifies a broad line, has, for example, $\Gamma/\omega_R \sim 3 \times 10^3$. In this case, Γ, or more generally the power-broadened linewidth Γ_E, is the natural energy scale. Here, $\Gamma_E = \Gamma\sqrt{1+s}$ is defined by the saturation parameter $s = I/I_S$ where I (I_S) is the single-beam peak intensity (transition saturation intensity). Semiclassical physics thus governs the cooling process and the photon recoil, although essential to

quantitatively understanding energy dissipation [13], serves more as a useful conceptual tool than a dominant player in system dynamics. Moreover, gravity is essentially negligible since the ratio of the maximum radiative force to the gravitational force, $R = \hbar k\Gamma/2mg$, is typically on the order of 10^5, where $2\pi\hbar$, k, m, and g are Plank's constant, the light field wave vector, the atomic mass, and the gravitational acceleration, respectively.

In contrast, narrow Doppler cooling lines are characterized by $\Gamma/\omega_R \sim 1$ or less. The 689 nm ^{88}Sr $^1S_0$-$^3P_1$ transition used in this work, for example, has $\Gamma/\omega_R = 1.6$ where $\Gamma/2\pi$ ($\omega_R/2\pi = \hbar k^2/4\pi m$) is 7.5 kHz (4.7 kHz). In this case, the relevant thermal-mechanical energy scale and thus the underlying semiclassical or quantum mechanical nature of the cooling depends on s. Details of a given cooling process are then set by the laser detuning $2\pi\delta = \Delta = \omega_L - \omega_A$ where ω_L (ω_A) is the laser (atomic resonance) frequency. In particular, $\delta < 0$ $^1S_0$-$^3P_1$ MOT dynamics can be divided into three qualitatively distinct regimes, hereafter labeled (I–III), defined by the relative size of $|\Delta|$, $\Gamma \sim \omega_R$, and Γ_E. In regime (III), corresponding to trapping beam intensities on the order of $I_S = 3$ μW/cm^2 or $s \sim 1$, ω_R is the natural energy scale. Here, single photon recoils and consequently, quantum physics, govern trap dynamics. This situation enables limiting temperatures of roughly half the photon recoil limit ($T_R = 2\hbar\omega_R/k_B = 460$ nK, where k_B is Boltzmann's constant) despite the incoherent excitation provided by the trapping beams [11,14].

Conversely, for $s \gg 1$ the system evolves toward semiclassical physics where $\Gamma_E \gg \omega_R$ and hence Γ_E is the dominant energy scale. In this case, cooling and motional dynamics are determined by the relative size of Γ_E and Δ. In regime (II), the $\Delta < \Gamma_E$ radiative force produces damped harmonic motion and, in analogy to standard Doppler cooling, MOT thermodynamics set entirely by the velocity dependence of the force [12,15]. For these conditions, the expected δ- and s-dependent temperature minima are observed, although with values globally smaller than standard Doppler theory predic-

———————
*Present address: Aculight Corporation, Bothell, WA 98011, USA. Email address: tloftus@aculight.com
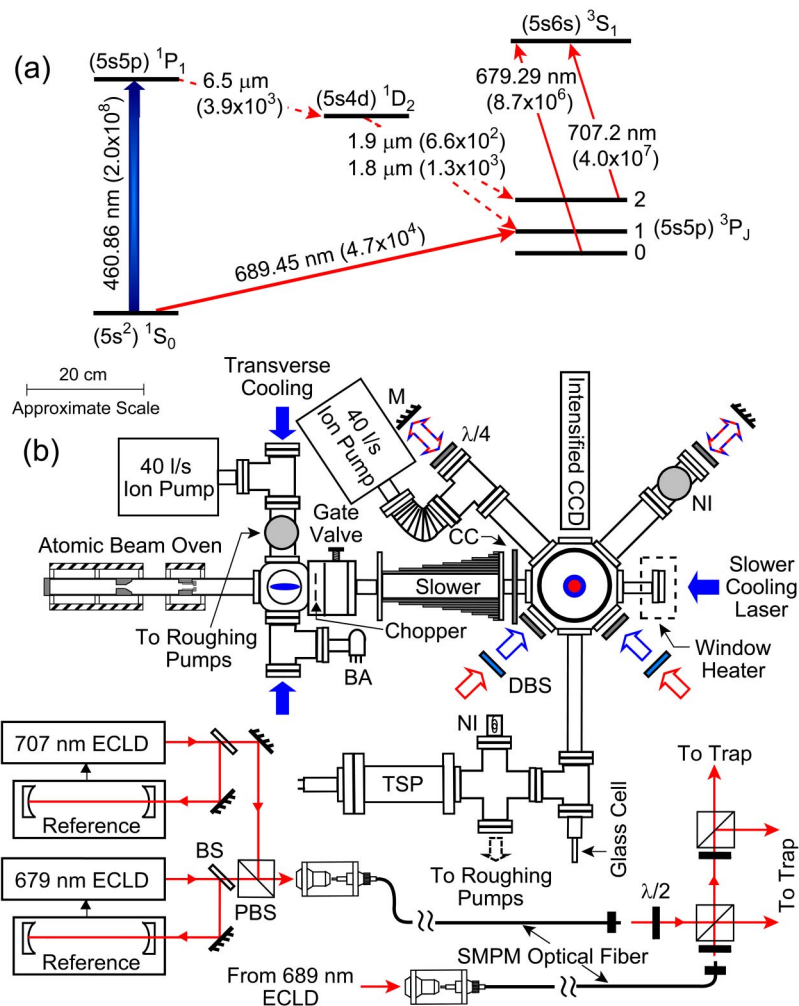†Email address: Ye@jila.colorado.edu

FIG. 1. (Color online) (a) Partial ^{88}Sr energy level diagram. Numbers in parentheses give Einstein A coefficients (in s^{-1}). Wavelengths are in vacuum. (b) Top (x-y plane) view of the Sr cooling and trapping apparatus. Blue (red) arrows represent 461 nm (689 nm, 679 nm, and 707 nm) trapping (trapping and repumping) beams. M, mirror; $\lambda/4$, dual wavelength quarter-wave plate; $\lambda/2$, half-wave plate; DBS, dichroic beamsplitter; PBS, polarization beamsplitter; BS, beamsplitter; SMPM, single-mode polarization maintaining; ECDL, external-cavity diode laser; BA, Bayard-Alpert vacuum gauge; NI, nude vacuum gauge; TSP, titanium sublimation pump; CC, compensation coil.

tions. Alternatively, in regime (I) where $\Delta > \Gamma_E$, the atom-light interaction is dominated by single-beam photon scattering and trap thermodynamics become intimately linked to both the velocity and the *spatial* dependence of the force. Here, gravity plays an essential role as the ratio R for the $^1S_0$-$^3P_1$ transition is only ~ 16. Consequently, the atoms sag to vertical positions where the Zeeman shift balances δ, leading to δ-independent equilibrium temperatures.

Narrow line cooling also displays a unique set of $\delta > 0$ thermal and mechanical dynamics. For these experiments, the atomic gas is first cooled to μK temperatures and then δ is suddenly switched from $\delta < 0$ to $\delta > 0$. Subsequently, the sample evolves from a thermal distribution to a discrete set of momentum-space packets whose alignment matches lattice points on a three-dimensional (3D) face-centered-cubic crystal [16]. Up to 26 independent packets are created with δ- and s-dependent lattice point filling factors. Note this surprising behavior occurs in the setting of incoherent excitation of a nondegenerate thermal cloud. To obtain qualitative insight into the basic physics, we begin with an analytic solution to the one-dimensional (1D) semiclassical radiative force equation. Here, we show that $\delta > 0$ excitation enables "positive feedback" acceleration that efficiently bunches the atoms into discrete sets of δ- and s-dependent velocity space groups. A simple generalization of the 1D model is then used

to motivate the experimentally observed 3D lattice structure. This intuitive picture is then confirmed with numerical calculations of the final atomic velocity and spatial distributions. Using the numerical calculations, we also show that $\delta > 0$ momentum-space crystals are a universal feature of standard Doppler cooling and that observations should be possible, although increasingly impractical, with broad line molasses.

Finally, we demonstrate that R directly influences $\delta > 0$ thermodynamics, enabling cooling around a δ- and s-dependent velocity v_0 where gravity balances the radiative force. Observed values for v_0 agree well with numerical predictions while cooling is evident in distinctly asymmetric cloud spatial distributions that appear in both numerical calculations of the cooling process and the experiment. As with momentum crystal formation, gravitationally assisted $\delta > 0$ cooling is universal to Doppler limited systems. In the more typical case where $R \sim 10^5$, however, equilibrium temperatures (v_0) are on the order of hundreds of milli-Kelvin (100 m/s) rather than the more useful micro-Kelvin (~ 10 cm/s) values achieved with narrow lines.

The remainder of this paper is organized as follows. Section II gives an overview of the 461 nm $^1S_0$-$^1P_1$ MOT used to precool ^{88}Sr to ~ 2.5 mK. $^3P_2$ metastable excited-state magnetic traps that are continuously loaded by the $^1S_0$-$^1P_1$

cooling cycle are also described. Section III details the highly stabilized 689 nm light source and the process used to transfer ^{88}Sr from the $^1S_0$-$^1P_1$ MOT to the $^1S_0$-$^3P_1$ MOT. Descriptions of the techniques used to control and study $^1S_0$-$^3P_1$ laser cooling are also provided. Sections IV and V then focus on $\delta < 0$ mechanical and thermal dynamics, respectively. Finally, Sec. VI explores $\delta > 0$ cooling and momentum-space crystals. Conclusions are given in Sec. VII.

II. $^1S_0$-$^1P_1$ MOT PRECOOLING

Pre-cooling ^{88}Sr to milli-Kelvin temperatures is an essential requirement for observing $^1S_0$-$^3P_1$ cooling and trapping dynamics [1]. For this purpose, as shown by Fig. 1(b), we use a standard six-beam 461 nm $^1S_0$-$^1P_1$ MOT that is loaded by a Zeeman slowed and transversely cooled atomic beam. The atomic beam is generated by an effusion oven (2 mm nozzle diameter) whose output is angularly filtered by a 3.6 mm diameter aperture located 19.4 cm from the oven nozzle. Separate heaters maintain the oven body (nozzle) at 525 °C (725 °C), resulting in a measured flux (divergence half-angle) of 3×10^{11} atoms/s (19 mrad).

The atomic beam is then transversely cooled by 2-dimensional 461 nm optical molasses. The elliptical cross-section, linearly polarized molasses laser beams have a $1/e^2$ diameter of ~ 3 cm (~ 4 mm) along (normal to) the atomic beam propagation axis, contain 10–20 mW of power, and are detuned from the $^1S_0$-$^1P_1$ resonance by −15 MHz. Stray magnetic fields in the transverse cooling region are less than 1 G. Subsequently, the atomic beam passes through a 6.4 mm diameter electromechanical shutter and a gate valve that allows the oven to be isolated from the rest of the vacuum system.

After exiting the transverse cooling region, the atomic beam enters a water cooled 20 cm long constant deceleration σ^- Zeeman slower [18] with a peak magnetic field of ~ 600 G, corresponding to a capture velocity of ~ 500 m/s. The 461 nm Zeeman slower cooling laser is detuned from the $^1S_0$-$^1P_1$ resonance by −1030 MHz, contains 60 mW of power, and is focused to approximately match the atomic beam divergence. The window opposite the atomic beam is a z-cut Sapphire optical flat that is vacuum sealed via the Kasevich technique [17], broadband anti-reflection coated on the side opposite the chamber, and heated to 200 °C to prevent the formation of Sr coatings. The alternating current window heater, which produces a small stray magnetic field, is only operated during the $^1S_0$-$^1P_1$ MOT precooling phase. A separate compensation coil reduces the slower magnetic field magnitude (gradient) to < 100 mG (< 8 mG/cm) at the trapping region, located 15 cm from the slower exit. Stray magnetic fields at the trap are further nulled by three sets of orthogonally oriented Helmholtz pairs.

The trapping chamber is a cylindrical octagon with six 2 3/4" (two 6 in.) ports in the horizontal x-y plane (along gravity z axis). All windows are broadband anti-reflection coated. The MOT anti-Helmholtz coils, oriented such that the axial magnetic field gradient $dB_z/dz = dB_z$ lies along gravity, are mounted on a computer controlled precision lin-

ear track that allows the coil center to be translated from the trapping chamber to a 1 cm × 1 cm × 4 cm rectangular glass cell. The coils are constructed to provide window-limited optical access to the geometric center of the trapping chamber and produce axial gradients of 0.819(4) G/(cm A). The gradient is linear over a spatial range of $\sim \pm 3$ cm in both the axial and transverse directions. Current in the coils is regulated by a computer controlled servo and monitored with a Hall probe. For the $^1S_0$-$^1P_1$ MOT, the axial magnetic field gradient $dB_z = 50$ G/cm.

The trapping chamber is evacuated by a 40 l/s ion pump and a titanium sublimation pump while the oven chamber uses a 40 l/s ion pump. The two chambers are separated by a 6.4 mm × 16 mm cylindrical differential pumping tube located between the electro-mechanical shutter and the gate valve. Typical vacuum levels in the oven, trapping, and glass cell chambers during operation of the atomic beam are 2 × 10^{-8} Torr, 1.5 × 10^{-9} Torr, and 3 × 10^{-10} Torr, respectively.

461 nm cooling and trapping light is produced by frequency doubling the output from a Ti:sapphire laser in two external buildup cavities [19] that together produce >220 mW of single-mode light. The 461 nm light is then offset locked to the $^1S_0$-$^1P_1$ resonance by saturated absorption feedback to the Ti:sapphire laser. Relative frequencies of the transverse cooling, Zeeman slower, and trapping laser beams are controlled with acousto-optic modulators (AOMs) which are also used as shutters. Additional extinction of 461 nm light is provided by electro-mechanical shutters. The intensity stabilized trapping beams have $1/e^2$ diameters of ~ 3 cm, are detuned from the $^1S_0$-$^1P_1$ resonance by −40 MHz, and typically have a total power of 30 mW. For these settings, we find the $^1S_0$-$^1P_1$ MOT population is maximized. Further increases in, for example, the trapping beam power simply increases the cloud temperature. $^1S_0$-$^1P_1$ MOTs are monitored with a charge-coupled-device (CCD) camera and a calibrated photodiode. Typical trap lifetimes, populations, and temperatures are 20 ms, 3×10^7, and 2.5 mK, respectively.

As shown by Fig. 1(a), operation of the $^1S_0$-$^1P_1$ MOT efficiently populates the ground-statelike $^3P_2$ metastable excited-state (~ 500 s radiative lifetime [20,21]) via $^1P_1 \rightarrow {}^1D_2 \rightarrow {}^3P_2$ radiative decay. Consequently, $^1S_0$-$^1P_1$ MOT loading times are typically limited to 10–50 ms [22–24]. To overcome this loss process, $^3P_2$ population is repumped to the $^1S_0$ ground-state via the $^3P_2 \rightarrow {}^3S_1 \rightarrow {}^3P_1 \rightarrow {}^1S_0$ channel by driving the 707 nm $^3P_2$-$^3S_1$ and 679 nm $^3P_0$-$^3S_1$ transitions with two external cavity diode lasers (ECDLs). Each laser is locked to a reference cavity that is simultaneously locked to a frequency stabilized helium neon laser. Double-passed AOMs are then used to tune the absolute laser frequencies. After passing through a single-mode polarization-maintaining optical fiber, the copropagating 707 nm and 679 nm laser beams are expanded to a $1/e^2$ diameter of ~ 1 cm and delivered to the $^1S_0$-$^1P_1$ MOT. An AOM located before the beam expansion optics allows for rapidly turning the beams either on or off (< 1 μs transition time). At the trap, the 707 nm (679 nm) beam contains 1.5 mW (2.5 mW) of power, resulting in an optical repumping time of
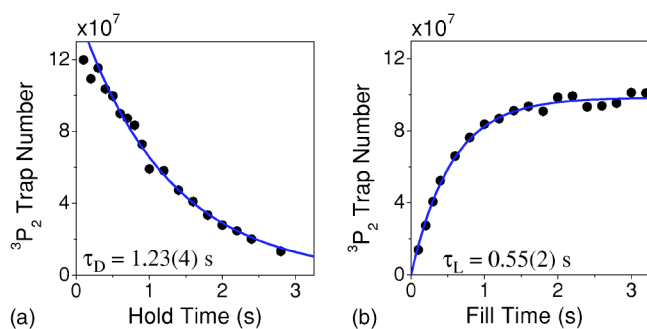
FIG. 2. $^3P_2$ magnetic trap population versus (a) hold time for a fixed 2 s loading time and (b) loading time at a hold time of 400 ms. Solid lines are exponential fits. $\tau_D(\tau_L)$ is the measured exponential decay (loading) time.

<100 μs. With both lasers operating, the $^1S_0$-$^1P_1$ MOT population and lifetime are typically enhanced by $10\times$ and $15\times$, respectively, with the former value limited by atomic beam induced trap loss.

Along with contributing to $^1S_0$-$^1P_1$ MOT loss, $^1P_1$ $\to$ $^1D_2$ $\to$ $^3P_2$ radiative decay continuously loads milli-Kelvin atoms in the $^3P_2(m=1,2)$ states into a magnetic trap formed by the $^1S_0$-$^1P_1$ MOT quadrupole magnetic field [24–30]. Importantly, these samples are expected to display a wealth of binary collision resonances that arise due to an interplay between anisotropic quadrupole interactions and the local magnetic field [31–33]. Qualitatively similar processes and hence, collision resonances, are predicted for polar molecules immersed in electrostatic fields [34]. Studies of metastable Sr collision dynamics will thus likely impact the understanding of a diverse range of physical systems. To pursue these studies, we plan to first load $^3P_2$ state atoms into the quadrupole magnetic trap and then mechanically translate [35] the sample to the glass cell chamber. Subsequently, a tight Ioffe-Pritchard magnetic trap will be used to perform a variety of collision experiments.

As a first step in this direction we have loaded $>10^8$ $^3P_2(m=1,2)$ state atoms into the quadrupole magnetic trap and achieved trap lifetimes >1 s. For these measurements, the $^3P_2$ trap is first loaded by operating the $^1S_0$-$^1P_1$ MOT for a variable fill time. The 461 nm cooling and trapping lasers and the atomic beam are then switched off. Following a variable hold time, the 461 nm trapping beams and the 707 nm and 679 nm repumping beams are switched on, enabling the $^3P_2$ magnetic trap population N_M to be determined from 461 nm fluorescence [26]. Figure 2(a) shows N_M versus hold time for a fill time of 2 s while Fig. 2(b) gives N_M versus fill time at a fixed hold time of 400 ms. For both, dB_z $=50$ G/cm, giving a magnetic trap depth of $\sim$30 mK. The $^1S_0$-$^1P_1$ MOT lifetime (steady-state population) is 16 ms (2.8×10^7). The observed 1.23(4) s exponential decay time agrees well with the expected $\sim$1.3 s vacuum limited value extrapolated from measurements reported in Ref. [28] at higher pressures. In contrast, the significantly shorter 0.55(2) s fill time implies that additional loss processes are operative during the loading phase, possibly due to interactions between atoms in the $^1D_2$ or $^3P_2$ states with $^1S_0$-$^1P_1$ MOT atoms or the atomic beam [30]. This idea is supported by the magnetic trap loading rate. For the parameters used here, the observed rate of $2.7(5)\times10^8$ atoms/s is $\sim2\times$ smaller than the theoretically predicted value of $5.4(1.8)$ $\times10^8$ atoms/s [25] where the theory only accounts for relevant branching ratios in the $^1P_1\to^1D_2\to^3P_2(m=1,2)$ radiative cascade. Similar discrepancies between observed and predicted loading rates were reported in Ref. [28].

III. $^1S_0$-$^3P_1$ MOT LOADING AND DETECTION

Exploring 689 nm $^1S_0$-$^3P_1$ narrow line cooling dynamics requires a laser system whose short-term linewidth is small compared to the 7.5 kHz transition natural width. In addition, the absolute laser frequency must be referenced, with similar stability, to the $^1S_0$-$^3P_1$ transition and be tunable over a range of $\sim$10 MHz. Figure 3 shows the 689 nm laser stabilization and control system consisting of a master-slave ECDL, a temperature stabilized and vibration isolated passive optical reference cavity, and a Sr saturated absorption spectrometer.

The linewidth of the master ECDL is first narrowed by locking the laser to a stable optical reference cavity via the Pound-Drever-Hall technique [36]. The cavity consists of high reflectivity Zerodour substrate mirrors that are optically contacted to a Zerodour spacer. The measured cavity finesse (free spectral range) at 689 nm is $\sim$3800 (488.9 MHz), giving a linewidth for the TEM$_{00}$ mode of $\sim$130 kHz. To isolate
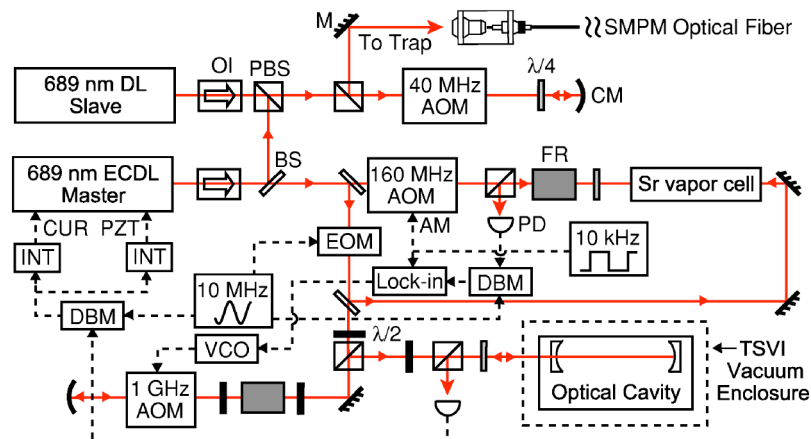

FIG. 3. (Color online) 689 nm laser system. Solid (dashed) lines are optical beams (electrical connections). $\lambda/4$, quarter-wave plate; $\lambda/2$, half-wave plate; M, mirror; CM, curved mirror; PBS, polarization beamsplitter; BS, beamsplitter; OI, optical isolator; FR, Faraday rotator; SMPM, single-mode polarization maintaining; ECDL, external-cavity diode laser; DL, diode laser; TSVI, temperature stabilized and vibration isolated; PD, photodiode; AOM, acousto-optic modulator; EOM, electro-optic modulator; DBM, double balanced mixer; INT, integrator; AM, amplitude modulation; CUR (PZT), current (piezoelectric mounted grating) modulation input.

the cavity from environmental perturbations, the cavity is suspended by two thin wires inside a temperature stabilized can that is evacuated to $<10^{-6}$ Torr and mounted on vibration damping material. The effective absolute cavity frequency is tuned by double-passing the 689 nm light sent to the cavity through a 1 GHz AOM. The electronic feedback, with an overall bandwidth of ~ 2 MHz is divided into a slow loop that adjusts the piezo-electric mounted ECDL grating and a fast loop that couples to the diode laser current. With the cavity lock engaged, in-loop analysis shows that jitter in the cavity-laser lock is <1 Hz.

To further evaluate the performance of the 689 nm laser system, the short-term laser linewidth is determined by beating the cavity-locked 689 nm light against a femto-second comb that is locked to a second optical cavity [37]. Here, we find a short-term linewidth of <300 Hz, where the measurement is limited by the optical fiber connecting the 689 nm light to the femto-second comb. Next, the absolute stability of the 689 nm laser is evaluated by beating the cavity locked 689 nm light against a femto-second comb that is locked to a Hydrogen maser via a fiber optical link to NIST [38]. From these measurements, the laser-cavity system drifts $\sim \pm 400$ mHz/s and has a 1 s stability of $<4 \times 10^{-13}$ (i.e., <180 Hz) with the former value limited by cavity drift and the latter value limited by the effective maser noise floor. To eliminate the slow cavity induced drift, the master ECDL is next locked to the $^1S_0$-$^3P_1$ resonance via saturated absorption feedback to the 1 GHz AOM. For added stability, a DC magnetic field is applied to the Sr vapor cell and the spectrometer is set to perform frequency modulation spectroscopy on the $^1S_0$-$^3P_1(m=0)$ transition. With the system fully locked, the 1 s stability is then $\sim 4 \times 10^{-13}$ while for time scales <5 min, the drift rate is $\sim \pm 10$ mHz/s. On longer time scales, baseline fluctuations in the error signal cause frequency excursions that are <1 kHz/day.

A portion of the 689 nm master ECDL output is next used to injection lock a 689 nm slave diode laser. The slave laser output, after double-passing through an AOM used for frequency shifting and intensity chopping, is then coupled into a single-mode polarization-maintaining optical fiber. Upon exiting the fiber, the 689 nm light, with up to 6 mW of power, is expanded to a $1/e^2$ diameter of 5.2 mm and divided into three equal intensity trapping beams. Dichroic beamsplitters are then used to co-align the 689 nm and 461 nm trapping beams. Trapping beam waveplates are $3\lambda/4$ ($\lambda/4$) at 461 nm (689 nm).

$^1S_0$-$^3P_1$ cooling and trapping dynamics are monitored either by *in situ* or time-of-flight (TOF) fluorescence images collected with an intensified CCD camera. The camera can view the cloud in either the horizontal x-y plane or nearly along gravity. The x-y plane (along gravity) images have a spatial resolution of 21 μm/pixel (37 μm/pixel). For *in situ* images, the 461 nm trapping beams are pulsed on for 10–50 μs immediately after the atoms are released from the trap while for TOF images, the atoms are allowed to first freely expand for a variable amount of time. We have verified that *in situ* images recorded with 461 nm pulses are identical to direct images of the in-trap 689 nm fluorescence aside from an improved signal-to-noise ratio. Typical TOF flight times are 20–35 ms. To determine cloud temperatures,
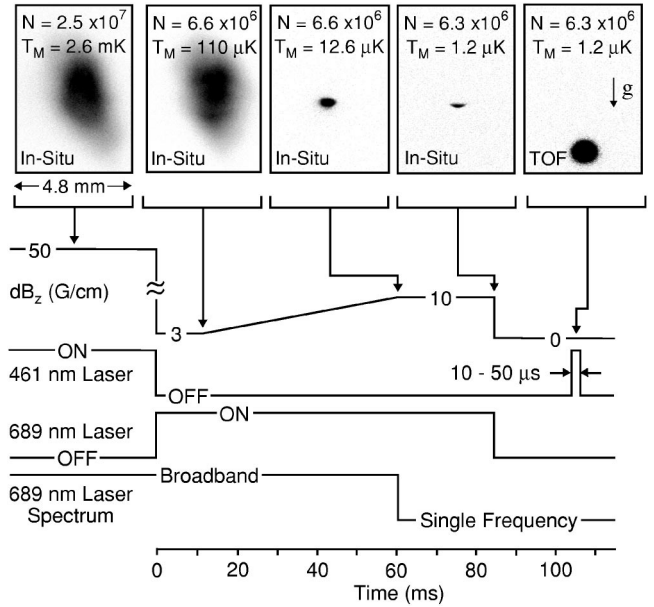

FIG. 4. $^1S_0$-$^3P_1$ MOT timing diagram. Images at top show the atomic cloud at each stage of the cooling and compression process. From left to right, the first four frames are *in situ* images while the last frame shows the cloud after 25 ms of free expansion from the $\delta=-520$ kHz, $s=75$ single-frequency MOT. N (T_M) is the cloud population (temperature).

Gaussian fits are performed to both the *in situ* and TOF images. The temperature T_M is then given by $T_M=(m/4k_Bt_F^2) \times (R_F^2-r^2)$ where t_F is the flight time and R_F (r) is the TOF (*in situ*) $1/e^2$ radius of the cloud.

Figure 4 depicts the $^1S_0$-$^3P_1$ MOT loading procedure [1]. As outlined in Sec. II, a $^1S_0$-$^1P_1$ MOT first precools $\sim 3 \times 10^7$ atoms to ~ 2.5 mK. At time $t=0$, the 461 nm light and the atomic beam shutter are switched off, dB_z is rapidly lowered to 3 G/cm, and red-detuned, broadband frequency modulated 689 nm trapping beams are turned on. 10 ms later and for the following 50 ms, the cloud is compressed by linearly increasing dB_z to 10 G/cm. Frequency modulation parameters for the 689 nm trapping beams are set to give complete spectral coverage of the $^1S_0$-$^1P_1$ MOT Doppler profile and, as shown below, manipulate the cloud size at the end of the magnetic field ramp. Subsequently, at $t=60$ ms, the frequency modulation is turned off and the atoms are held in a single-frequency MOT. As shown by the Fig. 4 images, transfer into the 689 nm MOT decreases the sample temperature by more than three orders of magnitude while only reducing the cloud population by a typical factor of 3–4, giving final sample temperatures of ~ 1 μK and populations of $\sim 10^7$. Typical single frequency trap lifetimes and spatial densities are ~ 1 s and $\sim 5 \times 10^{11}$ cm^{-3}, respectively. With 707 nm and 679 nm optical repumping of the $^1S_0$-$^1P_1$ MOT, the $^1S_0$-$^3P_1$ MOT population (spatial density) is typically 4×10^7 (3×10^{12} cm^{-3}). Optical repumping of the $^1S_0$-$^1P_1$ MOT, however, is not used in the remainder of this paper.

IV. $\delta<0$ MECHANICAL DYNAMICS

As outlined in Sec. I, $\delta<0$ $^1S_0$-$^3P_1$ MOTs provide a unique opportunity to explore three qualitatively distinct la-
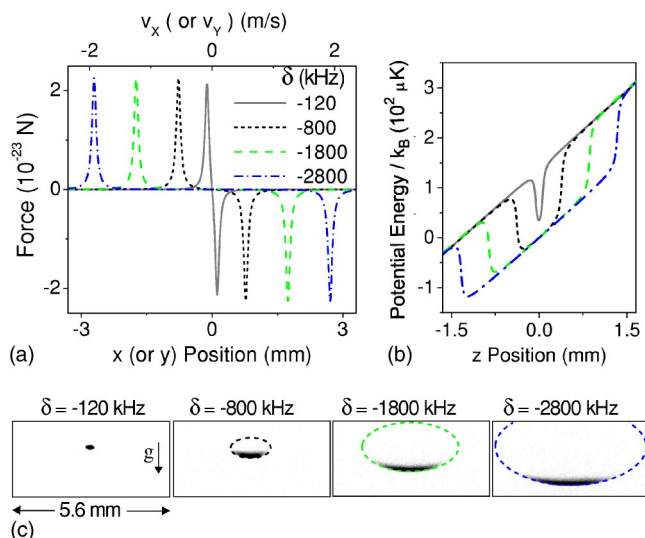
FIG. 5. (Color online). (a) Semiclassical radiative force versus position (bottom axis, $v_x=v_y=0$) and velocity (upper axis, $x=y=0$) for a range of detunings. Corresponding (b) trap potential energy in the z direction and (c) *in situ* images of the $^1S_0$-$^3P_1$ MOT. Dashed lines in (c) are calculated maximum force contours. For each, $s=248$.
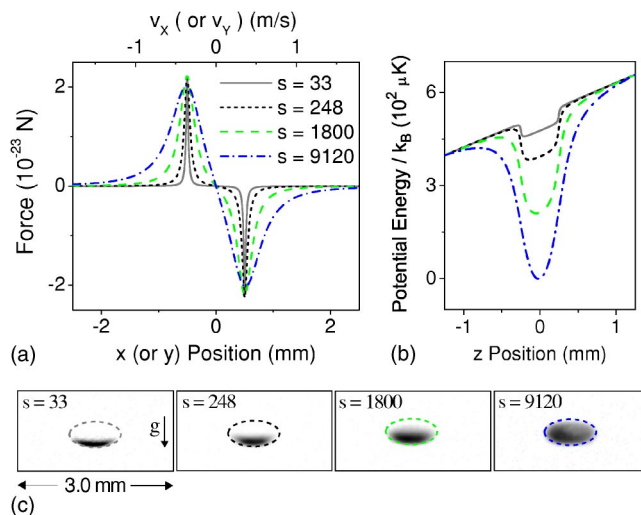

FIG. 6. (Color online) (a) Semiclassical radiative force versus position (bottom axis, $v_x=v_y=0$) and velocity (upper axis, $x=y=0$) for a range of intensities. Corresponding (b) trap potential energy in the z direction and (c) *in situ* images of the $^1S_0$-$^3P_1$ MOT. Dashed lines in (c) are calculated maximum force contours. For each, $\delta=-520$ kHz.

ser cooling regimes whose underlying mechanics are governed by either semiclassical or quantum mechanical physics. In this and the following section, we will describe the unique experimental signatures for regimes (I)–(III) and give detailed explanations for the observed trapped atom behavior.

Insight into regimes (I) and (II) thermal-mechanical dynamics is provided by the semiclassical radiative force equation [12]

$$\vec{F}(\vec{v},\vec{x}) = \frac{\hbar \vec{k} \Gamma}{2} \left[\frac{s}{1 + s' + 4(\Delta - \vec{k} \cdot \vec{v} - \mu d\vec{B} \cdot \vec{x})^2/\Gamma^2} - \frac{s}{1 + s' + 4(\Delta + \vec{k} \cdot \vec{v} + \mu d\vec{B} \cdot \vec{x})^2/\Gamma^2} \right] - m\vec{g},$$

(1)

where $\vec{x}=\{x,y,z\}$, $d\vec{B}=\{dB_x, dB_y, dB_z\}$, and $\mu=(g_J\mu_B/\hbar)$ where $g_J=1.5$ (μ_B) is the $^3P_1$ state Lande g-factor (Bohr magneton). $s'>s$ accounts, along a single axis, for saturation induced by the remaining four trapping beams. Figure 5(a) shows the $^1S_0$-$^3P_1$ radiative force at $s=s'=248$ for a range of δ values while Fig. 6(a) shows the force at $\delta=-520$ kHz for a range of $s=s'$ values. As described in Sec. I, the qualitative nature of the force and hence the resulting trap mechanical dynamics depends on the relative size of Δ and Γ_E. For regime (I), corresponding to $|\delta|>120$ kHz in Fig. 5(a) or $s<248$ in Fig. 6(a), $\Delta>\Gamma_E$ and the 3D radiative force acts only along a thin shell volume marking the outer trap boundary. Here, the trap boundary roughly corresponds to positions where the radiative force is peaked. This situation, as shown by Figs. 5(b) and 6(b), produces a box potential with a gravitationally induced z-axis tilt. Hence, in the x-y plane, motion

consists of free-flight between hard wall boundaries while along the z axis, mechanical dynamics are set by the relative size of the radiative force "kicks," gravity, and the cloud thermal energy. As shown in Sec. V, the thermal energy is small compared to the gravitational potential energy. Moreover, the ratio of the maximum radiative force to the gravitational force, $R \sim 16$. Thus, the atoms sink to the bottom of the trap where they interact, along the z axis, with only the upward propagating trapping beam.

As δ decreases in Fig. 5(a) or s increases in Fig. 6(a), the trap mechanically evolves to regime (II) where $\Delta < \Gamma_E$ produces a linear restoring force and hence, damped harmonic motion [12,15]. Consequently the trap potential energy assumes the U-shaped form familiar from standard broad line Doppler cooling. As the trap moves more fully into regime (II), perturbations to the potential energy due to gravity become less pronounced. One expects, therefore, that the cloud aspect ratio will evolve toward the 2:1 value set by the quadrupole magnetic field.

The intuitive descriptions developed above are directly confirmed by Figs. 5(c) and 6(c) which show *in situ* images of the $^1S_0$-$^3P_1$ MOT along with overlaid maximum force contours calculated from Eq. (1). For excitation conditions corresponding to regime (II), the cloud approaches the 2:1 quadrupole magnetic field aspect ratio. In contrast, for regime (I) the cloud x-y width is determined largely by the separation between x-y force maxima or alternatively, by the wall separation for the x-y potential energy box. In the vertical direction, the atoms sink to the bottom of the trap where the lower cloud boundary z_0 is defined by the location of the z-axis potential energy minima which is, in turn, proportional to the position where the Zeeman shift matches the laser detuning. As δ increases, z_0 shifts vertically downward, an effect predicted in Fig. 5(b) and clearly revealed in Fig. 5(c). To quantify this relationship, Fig. 7 shows z_0 versus δ along
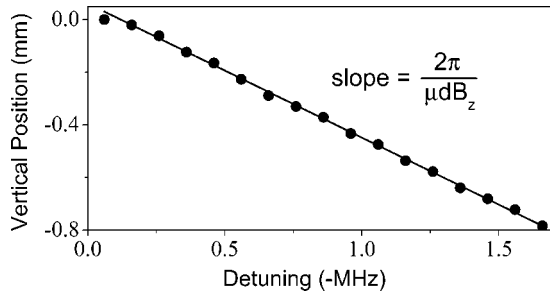
FIG. 7. Vertical cloud position versus δ for $s=248$ and $dB_z = 10$ G/cm. The solid line is a linear fit.

with a linear fit to the data giving $dz_0/d\delta = 2\pi/(\mu dB_z)$ $= 0.509(4)$ μm/kHz, in agreement at the 5% level with the expected linear slope of $0.478(2)$ μm/kHz.

Unique $^1S_0$-$^3P_1$ MOT mechanical dynamics are also manifest in the transfer efficiency between the broadband and single-frequency cooling stages. Here, it is important to note that following broadband cooling, the cloud vertical and horizontal $1/e^2$ radii (r_z and r_h, respectively) are set by the final value for dB_z and the spectral separation between the blue edge of the modulation spectrum and the $^1S_0$-$^3P_1$ resonance. Figure 8(a) shows three typical modulation spectra while Fig. 8(b) shows *in situ* images of the corresponding broadband cooled clouds at the end of the magnetic field ramp. For each, the measured temperature is 8.5(0.8) μK. Overlaid dashed lines give the maximum force contour for
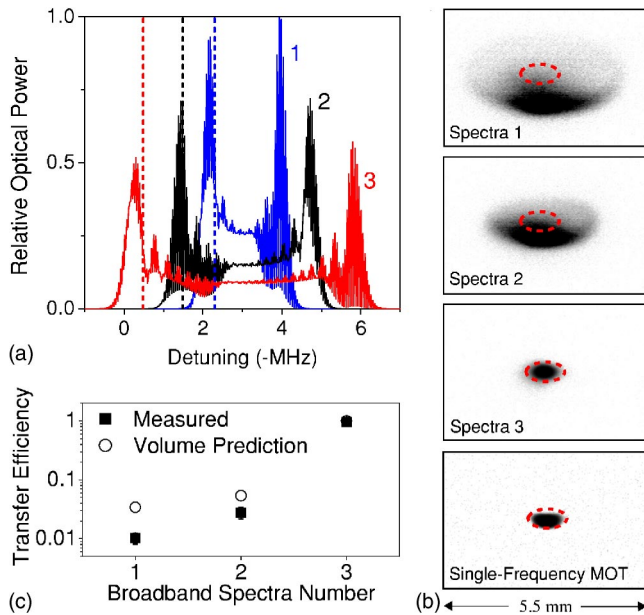

FIG. 8. (Color online). Modematching broadband cooled atoms to the single-frequency MOT. (a) Broadband modulation spectra. Dashed vertical lines give the effective detuning corresponding to the measured cloud size. (b) *In situ* images of the broadband cooled atoms. For each, the temperature is 8.5(0.8) μK. Dashed lines give the maximum force contour for the $\delta=-520$ kHz, $s=75$ single-frequency MOT shown in the bottom frame. (c) Broadband to single-frequency MOT transfer efficiency versus broadband spectra number.
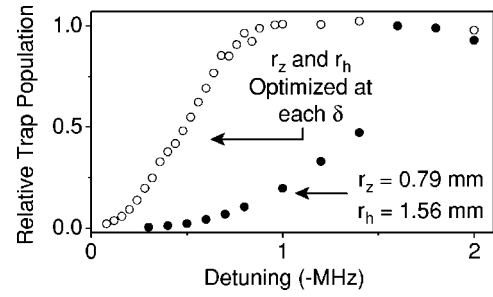

FIG. 9. Relative trap population versus δ when r_z and r_h are optimized at each point (open circles) or fixed at $r_z=0.79$ mm and $r_h=1.56$ mm (solid circles). For both, $s=248$ and $dB_z=10$ G/cm.

the subsequent $\delta=-520$ kHz, $s=75$ single-frequency MOT shown in the bottom frame. Here, dynamics similar to Fig. 5 are observed: as the broadband modulation moves closer to resonance, the cloud density distribution becomes more symmetric and the aspect ratio evolves toward 2:1. Figure 8(c) shows the broadband to single-frequency MOT transfer efficiency TE versus broadband spectra number. Clearly, TE increases as the overlap between the broadband cooled cloud and the single-frequency MOT force contour increases, indicating that TE can be optimized by "mode-matching" r_z and r_h to the single-frequency MOT box. This idea is supported by open circles in Fig. 8(c) which give predicted TE values based on the relative volume of the broadband cooled cloud and the single-frequency radiative force curve. Overall, the prediction reproduces observed TE values with a discrepancy for spectra 1 and 2 that likely arises from the broadband MOT density distribution.

Further evidence for broadband to single-frequency mode-matching is provided by the single-frequency MOT population N versus δ shown in Fig. 9. Here, solid circles give N versus δ when $r_z=0.79$ mm and $r_h=1.56$ mm. According to the Fig. 5 model, the single-frequency MOT acquires these dimensions at $\delta=-1637$ kHz, which lies within 2% of the δ value where N is peaked. Hence, we again find that optimal transfer occurs when r_z and r_h are matched to the single-frequency radiative force contour. Additional confirmation for this effect is provided by open circles in the figure which give N when r_z and r_h are optimized at each δ. To understand the trend in this case toward smaller N as δ decreases, note the finite slope for the blue edge of the modulation spectrum sets the minimum effective detuning δ_m that can be used during the broadband cooling phase. In analogy to Fig. 5, δ_m sets minimum values for r_z and r_h. Thus mode-matching becomes progressively more difficult as δ decreases and the single-frequency radiative force contour shrinks, leading to the observed decrease in N.

V. $\delta<0$ THERMODYNAMICS

$\delta<0$ $^1S_0$-$^3P_1$ MOTs display a rich variety of thermodynamic behaviors that are directly linked to the mechanical dynamics explored in Sec. IV. Figure 10(a) shows the MOT equilibrium temperature T_M versus δ for saturation parameters ranging from $s=7.5$ to $s=1800$. For large δ and s, corresponding to regime (I) where $\Delta>\Gamma_E \gg \Gamma$, T_M is basically
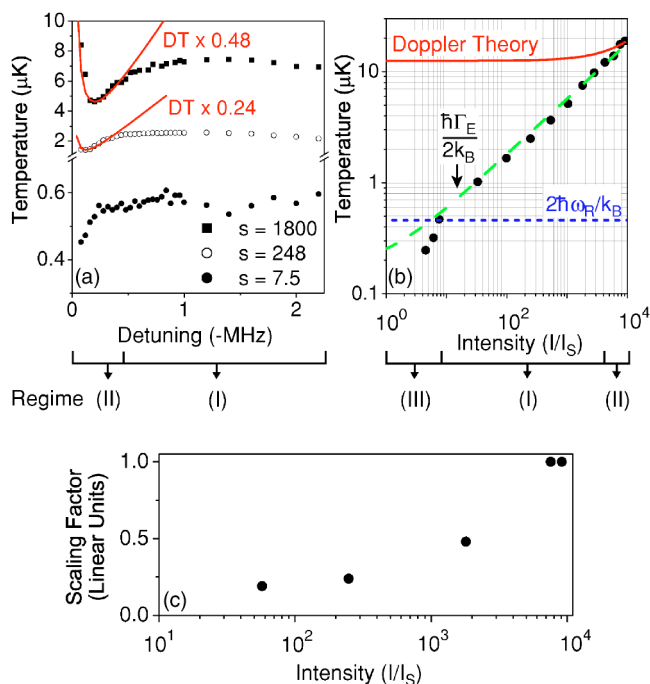
FIG. 10. (Color online) $^1S_0$-$^3P_1$ MOT temperature versus (a) detuning δ for various intensities and (b) intensity s at $\delta=$ −520 kHz. In (a), DT is standard Doppler theory. In (b), solid circles are experimental data while the solid, dashed, and short dashed lines give standard Doppler theory, the Doppler limit ($\hbar\Gamma_E/2k_B$), and the single-photon recoil limit ($2\hbar\omega_R/k_B$), respectively. (c) Global scaling factor applied to Doppler theory in order to match regime (II) data versus intensity.

δ-independent. Insight into this behavior is provided by Fig. 11(a), which details the unique regime (I) connections between trap thermodynamics, the spatial dependence of the radiative force, and the relative size of the radiative force and gravity. Recall that for $\Delta > \Gamma_E$, the cloud sags to the bottom of the trap where interactions occur, along the vertical z-axis, with only the upward propagating trapping beam. Moreover, due to polarization considerations and the free-flight motion executed by atoms in the horizontal plane, horizontal beam absorption rates are more than $4\times$ smaller than the vertical
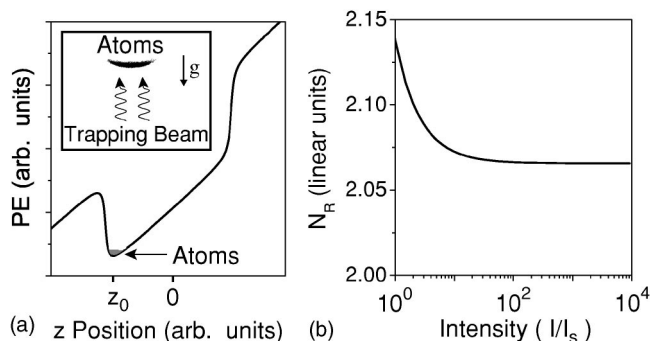

FIG. 11. (a) Schematic depiction of regime (I) cooling. Atoms sag to the bottom of the potential energy (PE) curve where interactions occur primarily with the upward traveling trapping beam. The inset shows the excitation geometry. (b) Numerical factor N_R in Eq. (6) versus intensity.

rate. Trap thermodynamics, therefore, are dominated by a balance between gravity and the radiative force due to the upward propagating beam. Here, it is important to realize that as δ changes, the z-axis atomic position z_0 self adjusts such that the effective detuning, $\Delta - \mu dB_z z_0$, remains constant. Consequently the trap damping and diffusion coefficients, and thus the equilibrium temperature, remain constant.

To obtain a quantitative expression for T_M under these conditions, we first find the damping coefficient α by Taylor expanding the semiclassical force expression

$$F(v_z,z) = \frac{\hbar k \Gamma}{2}\left[\frac{s}{1 + s' + \frac{4(\Delta - kv_z - \mu dB_z z)^2}{\Gamma^2}}\right] - mg, \quad (2)$$

where $(\partial F/\partial v) = \alpha$ is evaluated at $v_z = 0$, $z = z_0$. Solving $F(0,z_0) = 0$ and using $R = (\hbar k \Gamma/2mg)$, the δ-independent effective detuning is given by

$$\frac{\Delta - \mu dB_z z}{\Gamma} = -\frac{\sqrt{Rs - s' - 1}}{2}, \quad (3)$$

which, in combination with Eq. (2), states that the scattering rate depends only on R, s, and Γ. Substituting this expression into $(\partial F/\partial v)$, we obtain the damping coefficient

$$\alpha = -\frac{2\hbar k^2 \sqrt{Rs - s' - 1}}{R^2 s}. \quad (4)$$

Next, the diffusion coefficient D_p is calculated by substituting Eq. (3) into the single-beam scattering rate. D_p is then given by

$$D_p = \frac{\hbar^2 k^2 \Gamma}{2R}. \quad (5)$$

Combining Eqs. (4) and (5), the predicted δ-independent equilibrium temperature is

$$T = \frac{D_p}{|\alpha|} = \frac{\hbar \Gamma \sqrt{s}}{2k_B} \frac{R}{2\sqrt{R - s'/s - 1/s}} = \left(\frac{\hbar \Gamma_E}{2k_B}\right)N_R, \quad (6)$$

where we have used $\sqrt{s} \sim \sqrt{s+1}$ for $s \gg 1$. As shown by Fig. 11(b), the numerical factor N_R is approximately 2 over the entire relevant experimental range. Regime (I) temperatures, therefore, depend only on Γ_E. To test this prediction, Fig. 10(b) shows T_M versus s for a fixed large detuning $\delta=$ −520 kHz. For the central portion of the plot where regime (I) dynamics are relevant, we find good agreement with Eq. (6) aside from a global scaling factor of two.

For small δ in Fig. 10(a), the system evolves from regime (I) to regime (II) where $\Delta < \Gamma_E$, $\Gamma_E \gg \Gamma$. As this transition occurs, trap dynamics change from free-flight to damped harmonic motion. Here, one expects thermodynamics similar to ordinary Doppler cooling including δ- and s-dependent minima with equilibrium values having the functional form [12,15]

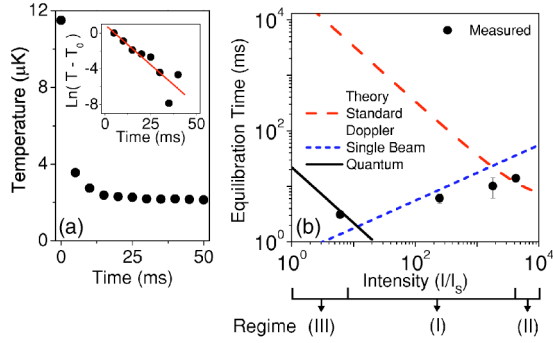$$T(s,\Delta) = T_0(4|\Delta|/\Gamma_E)^{-1}[1 + 4(\Delta/\Gamma_E)^2],$$

FIG. 12. (Color online) The approach to thermal equilibrium at $\delta=-520$ kHz. (a) Measured temperature versus time for $s=248$. The inset gives a semilog plot for times greater than 5 ms. The solid line is a linear fit. T, instantaneous temperature; T_0, final equilibrated temperature. (b) Measured exponential equilibration time versus s. The dashed, short dashed, and solid lines are predictions from standard Doppler theory, the single-beam theory outlined in the text, and quantum theory, respectively.

$$T_0 = (\hbar\Gamma_E)/(2k_B), \qquad (7)$$

where T_0, realized at $\Delta=\Gamma_E/2$, is a generalized version of the $s\ll 1$ Doppler limit. As shown by the solid lines in Fig. 10(a), Eq. (7) correctly reproduces the functional shape of the data. As shown by Fig. 10(c), however, matching the absolute data values requires multiplying Eq. (7) by a s-dependent global scaling factor (≤ 1) whose value decreases with s, leading to temperatures well below the standard Doppler limit T_0. In contrast to ordinary Doppler cooling, the cloud thermal energy in regime (II) is thus not limited by half the effective energy width of the cooling transition. Notably, we find this surprising result cannot be explained either by analytic treatments of Eq. (1) or semiclassical Monte Carlo simulations of the cooling process. The Monte Carlo simulations, in fact, simply reproduce standard Doppler theory. Finally, as s approaches unity in Fig. 10(b), the trap enters regime (III) where $\Gamma \sim \omega_R \sim k_B T/\hbar$ and thus the cooling becomes fully quantum mechanical. Here, we obtain a minimum temperature of 250(20) nK, in good agreement with the quantum mechanically predicted value of half the photon recoil temperature $T_R/2 = \hbar\omega_R/k_B = 230$ nK [14].

The approach to thermal equilibrium also displays signatures of regimes (I)–(III). Figure 12(a) gives the cloud temperature versus time following transfer from the broadband cooling stage to a $\delta=-520$ kHz, $s=248$ single-frequency MOT. As shown by the figure inset, the data is well fit by a single exponential aside from the rapid decrease for times <5 ms that arises from atoms falling outside the trap capture velocity [8,9]. Recall from Fig. 10 that scanning s at this detuning provides access to all three cooling regimes, each of which is characterized by a unique evolution toward thermal equilibrium. Specifically, for regimes (I) and (II), semiclassical Doppler theory predicts an equilibration time $\tau = m/2|\alpha|$ where α is given in regime (I) by Eq. (4) and, according to ordinary Doppler theory, in regime (II) by [12,15]

$$\alpha = -\frac{4\hbar k^2}{3}\frac{|\Delta|}{\Gamma}\left[\frac{s}{1+s'+4(\Delta/\Gamma)^2}\right]. \qquad (8)$$

Conversely, quantum theory predicts that for regime (III), τ follows [14]

$$\tau \sim \frac{(k_B T_i)^2}{\hbar^2\Gamma^3 s}, \qquad (9)$$

where T_i is the initial cloud temperature. As a test of these predictions, Fig. 12(b) shows τ versus s at $\delta=-520$ kHz along with τ values predicted by the above three theories. Note that for each s value we find the temperature versus time is well fit by a single exponential aside from the ~ 5 ms long rapid decrease typified by Fig. 12(a). In regime (II) at $s=4520$, $\tau=14(2)$ ms, in good agreement with Doppler theory which gives $\tau \sim 12$ ms. As expected for regime (I), corresponding to $10 < s \leq 4000$, τ follows equilibration times predicted by the single-beam damping coefficient while in regime (III) at $s=6.1$, $\tau=3.1(4)$ ms, consistent with the Eq. (9) quantum mechanical predictions.

VI. $\delta>0$ COOLING AND MOMENTUM-SPACE CRYSTALS

Tuning to $\delta>0$ during the single-frequency cooling stage reveals two fundamental and unique physical processes: (1) the creation of well-defined momentum packets whose velocity space alignment mimics lattice points on a face-centered cubic crystal and (2) laser cooling around a velocity v_0 where the radiative force balances gravity. In the following, we explore these two effects in detail.

Basic insight into $\delta>0$ momentum packet formation can be obtained by considering the elementary problem of 1D atomic motion in the presence of two counter-propagating $\delta>0$ light fields. For simplicity, we assume $d\vec{B}=0$. According to Eq. (1), an atom with initial velocity $\vec{v}_i$ will preferentially interact with the field for which $\vec{k}\cdot\vec{v}_i>0$. Hence, the absorption process tends to accelerate rather than decelerate the atom, further decreasing the probability for absorption events that slow the atomic motion and enabling "positive feedback" in velocity space. This process terminates for final velocities v_f satisfying

$$v_f \gg \frac{1}{k}\left(\Delta + \frac{\Gamma\sqrt{1+s}}{2}\right), \qquad (10)$$

which has a linear Δ dependence and scales with Γ_E. Neighbor atoms with initial velocities around $\vec{v}_i$ undergo similar "positive feedback" acceleration and ultimately achieve final velocities near v_f. To quantify this latter effect, we first simplify the problem by neglecting the beam for which $\vec{k}\cdot\vec{v}_i < 0$. The equation of motion for the atomic velocity is then

$$\frac{\partial v}{\partial t} = \frac{\hbar k\Gamma}{2m}\left[\frac{s}{1+s+\dfrac{4(\Delta-kv)^2}{\Gamma^2}}\right], \qquad (11)$$

which can be solved analytically for the interaction time t as a function of the velocity v
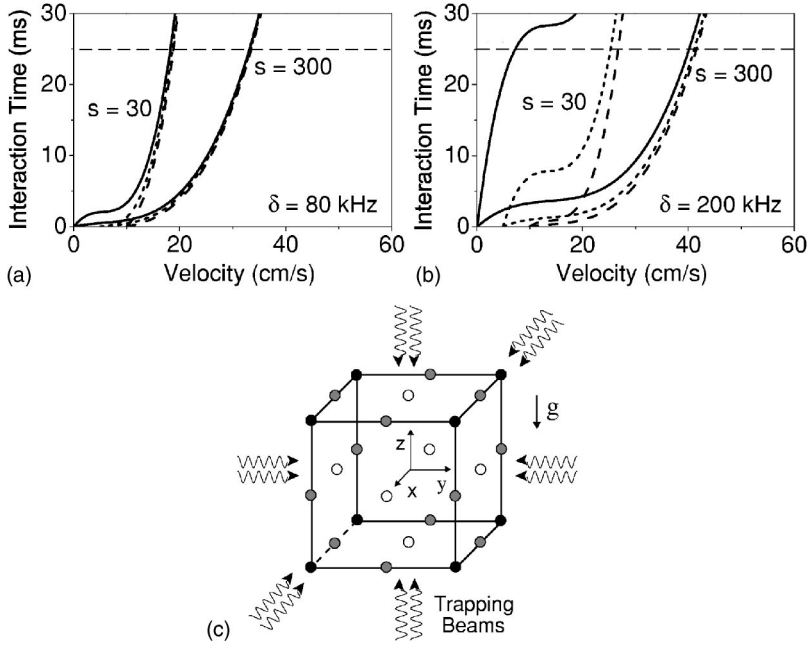
FIG. 13. One dimensional velocity bunching due to single-beam $\delta > 0$ absorption for (a) $\delta = 80$ kHz and (b) $\delta = 200$ kHz. Solid, short dash, and dashed lines correspond to initial velocities of 0.1 cm/s, 5 cm/s, and 10 cm/s, respectively. (c) Three-dimensional $\delta > 0$ momentum space structure. Final momenta corresponding to the black, gray, and white circles arise from three-, two-, and single-beam interactions, respectively.

$$t(v,v_i) = \frac{2m}{\hbar k s \Gamma^3}\left[\frac{4}{3}k^2 v^3 - 4\Delta k v^2 + [(1+s)\Gamma^2 + 4\Delta^2]v\right.$$

$$\left. - \frac{4}{3}k^2 v_i^3 - 4\Delta k v_i^2 + [(1+s)\Gamma^2 + 4\Delta^2]v_i\right]. \quad (12)$$

Figures 13(a) and 13(b) show plots of Eq. (12) at $\delta = 80$ kHz and $\delta = 200$ kHz, respectively. For both, $s = 30$ or $s = 300$. The chosen v_i values of 0.1 cm/s, 5 cm/s, and 10 cm/s span the velocity distribution for a 12 μK cloud. Assuming an interaction time of 25 ms, Fig. 13(a) clearly shows that due to laser induced acceleration, the entire range of initial velocities is rapidly bunched to a significantly reduced range of final velocities. Considering a fully 1D situation, this result implies the cloud is divided into two well defined and oppositely moving packets. As δ increases to 200 kHz in Fig. 13(b), the $s = 30$ atom-light interaction becomes sufficiently weak for $v_i \sim 0$ that two final velocity groups centered around $v_f \sim 8$ cm/s and $v_f \sim 25$ cm/s appear. In contrast, we find that for $s = 300$ the transition to two groups does not occur until $\delta \sim 400$ kHz. Accounting again for the full 1D symmetry, the $s = 30$ case corresponds to dividing the $t = 0$ cloud into three groups, two that move in opposite directions with relatively large final velocities and one that, in comparison, is nearly stationary. Overall, Eq. (11) thus predicts that for $\delta > 0$ the atomic cloud evolves into a discrete set of momentum-space packets. As s decreases at fixed δ, the number of packets increases while, as predicted by Eq. (10), the mean velocity for a given packet scales with both δ and s.

Generalizing this analysis to the full 3D molasses beam geometry leads to the structure shown in Fig. 13(c): a 3D array of momentum-space groups whose alignment mimics the lattice points on a face-centered-cubic crystal. Given the linear mapping between momentum and position space, this structure can be directly observed in position space. From symmetry considerations, cube corners correspond to three

beam interactions in which the cloud is divided into two pieces along each coordinate axis. According to Figs. 13(a) and 13(b), these points have a δ- and s-dependent mean velocity and appear at relatively small detunings. For larger δ values, two-beam interactions fill points along the Fig. 13(c) corner connecting lines. In analogy to $s = 30$ in Fig. 13(b), atoms in these points have $v_i \sim 0$ along a single axis and thus remain nearly stationary along that axis. Along the remaining two axes, however, $v_i > 0$, enabling acceleration to larger v_f. The 3-beam to 2-beam transition, as shown in Figs. 13(a) and 13(b), occurs at progressively larger δ values as s increases. Together, the two processes form a total of 20 divided groups with 8, 4, and 8 packets in the top, middle, and bottom layers of the cube, respectively. Finally, as δ increases further, atoms with $v_i \sim 0$ along two axes experience acceleration only along the remaining axis, producing the 1-beam lattice points shown as 6 open circles in the Fig. 13(c) cube face centers.

Figure 14 shows an array of top view (slightly off vertical) *in situ* cloud images for intensities ranging from $s = 30$ to $s = 1040$ and detunings spanning $\delta = 80$ kHz to $\delta = 200$ kHz. For each, $|\vec{dB}| = 0$ and the atom-light interaction time is fixed at $t_H = 25$ ms ($t_V = 25$ ms) in the horizontal x-y plane (along z-axis) molasses beams. The initial $t_H = t_V = 0$ cloud temperature is 11.5(2) μK. Here, the observed cloud evolution agrees well with the qualitative predictions developed from the Fig. 13 model. As δ increases at fixed s, sets of n-beam lattice points sequentially fill with $n = 3$ filling first followed by $n = 2, 1$. Moreover, as s increases, transitions between the n-beam processes occur at progressively larger δ values. Finally, for fixed δ, the mean lattice point velocity, proportional to the resulting lattice point spacing in the Fig. 14 images, scales with s as expected from both Eq. (10) and Fig. 13. Note that qualitatively similar dynamics are observed for $|\vec{dB}| \neq 0$. The detailed changes to the cloud evolution that result from this situation are described below.

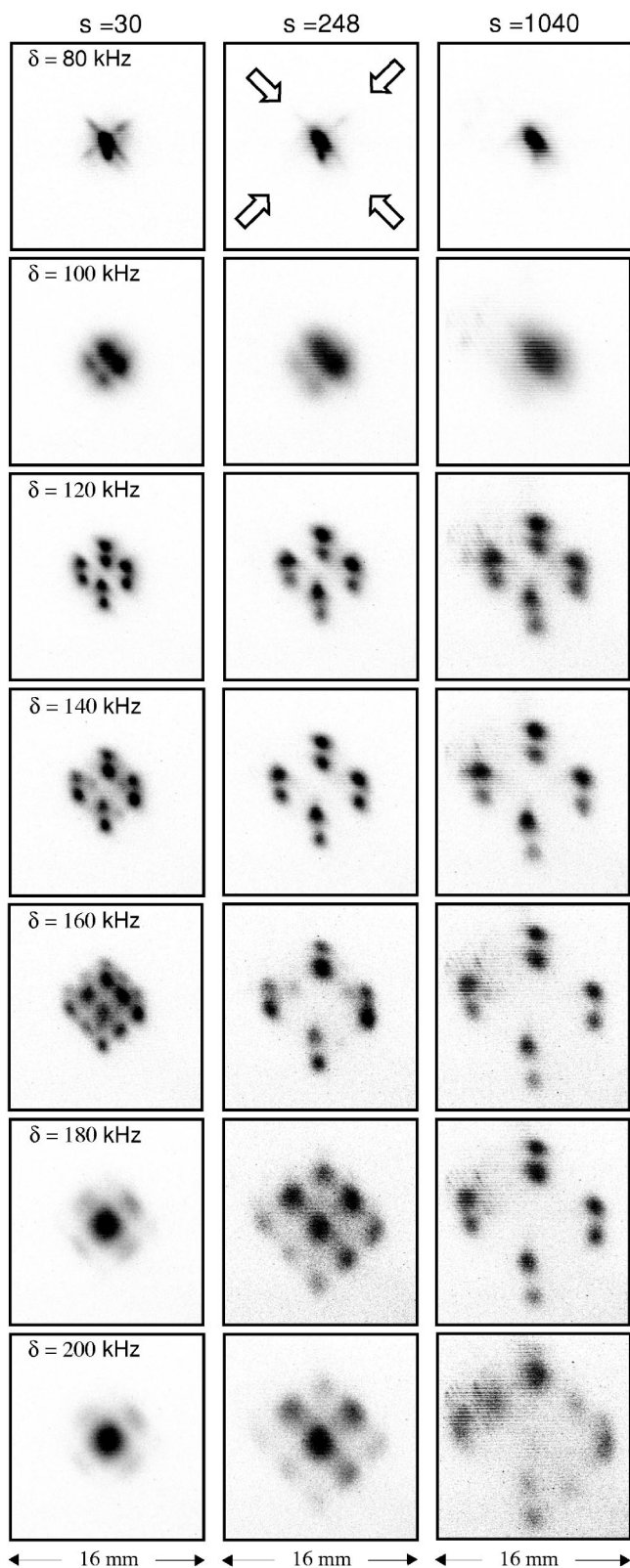FIG. 14. Top view (tilted slightly relative to gravity) *in situ* images for a range of δ and s at $|\vec{dB}|=0$ and $t_H=t_V=25$ ms. Arrows in the uppermost center frame show the propagation direction for the horizontal molasses beams. Note the horizontal beams are not completely orthogonal to the field of view. The initial cloud temperature is 11.5(2) μK.
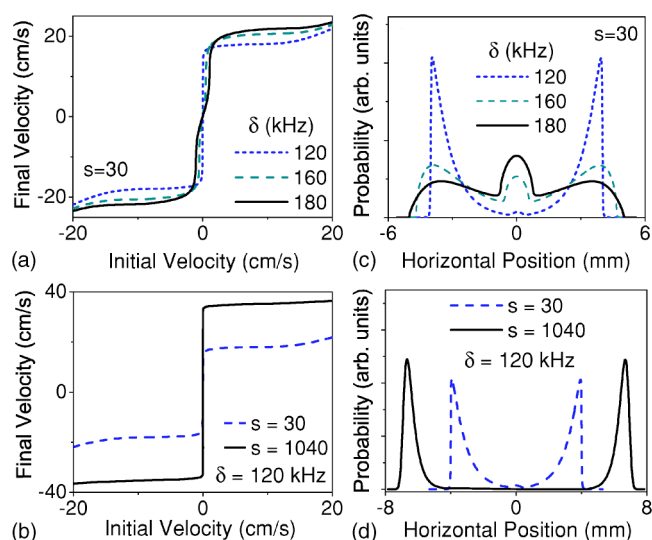

FIG. 15. (Color online) Calculated horizontal $\delta>0$ final versus initial velocity for (a) various δ at $s=30$ and (b) various s at $\delta=120$ kHz. (c) and (d) give the corresponding spatial distributions. For each, $t_H=25$ ms and the $t_H=0$ temperature is 11.5 μK.

The intuitive understanding of $\delta>0$ dynamics developed above is confirmed by Fig. 15. Here, we show numerical calculations based on Eq. (1) of the final horizontal velocity and spatial distributions for the $s=30$ column and $\delta=120$ kHz row in Fig. 14. For the calculations, $|\vec{dB}|=0$, $t_H=25$ ms, and the initial cloud temperature is 11.5 μK. The Figs. 15(c) and 15(d) spatial distributions should be compared to cube lines in the x-y plane along the Fig. 14 x-y molasses beam propagation directions. Importantly, this fully 1D model reproduces both the Fig. 14 observations and the Fig. 13 predictions for the δ- and s-dependent lattice point filling factors and mean lattice point velocity. As expected, the temperature of each packet in its moving frame is lower than the $t_H=t_V=0$ ms atomic cloud, a result arising from the previously described velocity bunching effects and directly connected to cloud shape asymmetries observed in both the experiment (note the sharp outer cloud edges) and the Fig. 15 theory. Notably, however, only two vertical layers are observed in Fig. 14 while the Fig. 13 model predicts three. As explained below, this apparent discrepancy arises from novel gravitationally induced z-axis dynamics.

At this point, it is important to realize that Eq. (1) is semiclassical and thus does not account for dynamics that depend on the relative size of Γ and ω_R. The $\delta>0$ momentum crystals observed here, therefore, are a universal feature of Doppler limited systems. Similar processes should then occur with broad lines such as the 461 nm $^1S_0$-$^1P_1$ transition. To test this possibility, Fig. 16 shows numerically simulated final horizontal velocity and spatial distributions for a 2.5 mK ^{88}Sr cloud excited by 461 nm $\delta>0$ optical molasses. For the calculation, $|\vec{dB}|=0$, $t_H=500$ μs, and $s=2$. As clearly indicated by the figure, structures very similar to those shown in Fig. 14 can be generated over length scales consistent with 461 nm cooling beam diameters and typical $^1S_0$-$^1P_1$ MOT temperatures. Moreover, we find that by increasing either s or t_H, structures with contrast identical to those
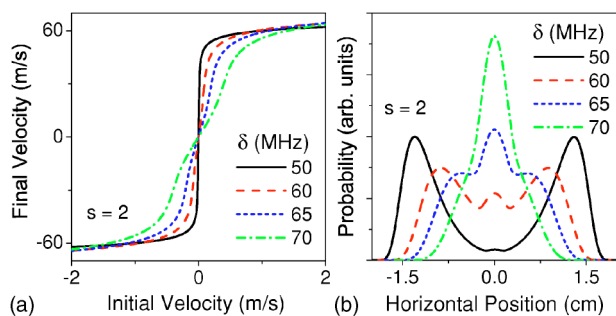
FIG. 16. (Color online) Broad line momentum space crystals. Calculated horizontal (a) final versus initial velocity and (b) corresponding spatial distributions for 461 nm $\delta=0$ optical molasses. For each, $t_H=500$ μs and the initial temperature is 2.5 mK.

shown in Figs. 14 and 15 can be created. Note the model does not account for spontaneous emission induced random walk heating, a process the would tend to smear the contrast between individual momentum packets. This omission, however, should not significantly affect Fig. 16 since random walk heating scales as $\sqrt{\Gamma}$ [12] while, from Eq. (1), the directional acceleration scales as Γ. Thus, as Γ increases from the narrow to the broad line case, random walk heating becomes progressively less important.

Although the physics underlying $\delta>0$ momentum-space crystals is thus fully operative for broad lines, details of the crystal formation process will make experimental observations difficult. From Eq. (10), v_f for a given packet is proportional to Γ. Hence, broad line packet velocities are orders of magnitude larger than achieved in the narrow line case. In Fig. 16, for example, $v_f\sim\pm60$ m/s. Visualizing the entire structure then requires imaging light with an optical bandwidth of ~260 MHz or an equivalently broad optical transition. This situation should be compared to the experiments performed here where $v_f<1$ m/s, and hence sufficient imaging bandwidth is obtained with the $\Gamma/2\pi=32$ MHz $^1S_0$ $-^1P_1$ transition. In addition, Γ sets the lattice point spacing, or alternatively the molasses beam diameter required to achieve a given contrast between individual lattice points. For the contrast shown in Figs. 14 and 15 for example, the required broad line molasses beam diameters grow to tens of centimeters, making experimental observations impractical.

Figure 17(a) shows *in situ* images of the 689 nm $\delta>0$ molasses when the cloud is viewed in the horizontal *x-y* plane at 45° to the *x-y* axes. For the images, $|d\vec{B}|=0$, $s=30$, $\delta=140$ kHz, $t_H=25$ ms, and t_V is varied from $t_V=0$ ms to $t_V=25$ ms. Here, the apparent contradiction between Fig. 14 and the Fig. 13(c) prediction for the number of vertical layers is shown to occur due to gravity induced dynamics. Increasing t_V from $t_V=0$ ms to $t_V=6$ ms, for example, creates three vertical layers, as predicted by Fig. 13(c). For $t_V>6$ ms, however, the lower two layers slowly merge together, becoming a single cloud along the vertical direction for $t_V>21$ ms. To understand this process, recall that the central layer in the Fig. 13(c) cube corresponds to atoms with near zero *z*-axis velocities. For the chosen δ and in the absence of gravity, these atoms remain near $v_z=0$. As shown by the numerical calculations in Figs. 17(b) and 17(c),
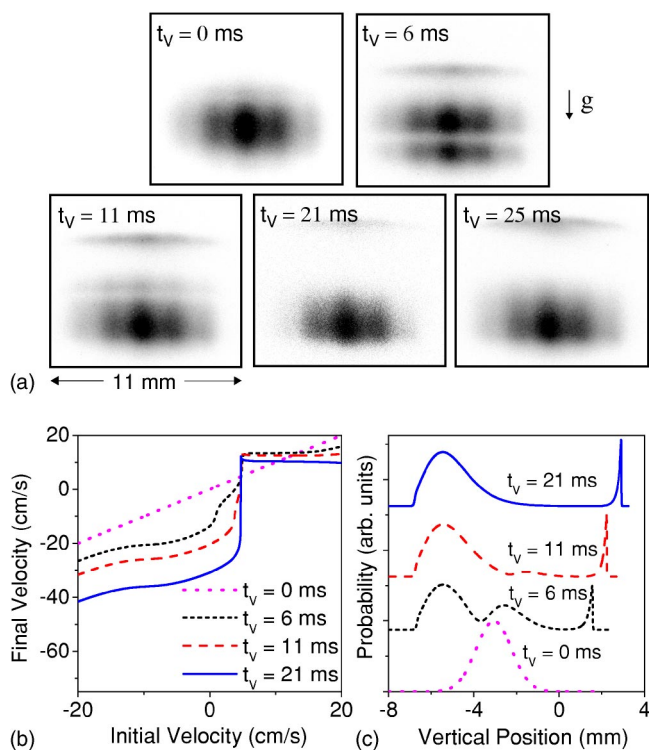

FIG. 17. (Color online) Side view *in situ* images for $s=30$, $|d\vec{B}|=0$, $\delta=140$ kHz, $t_H=25$ ms, and a range of t_V times. The $t_H=t_V=0$ cloud temperature is 11.5(2) μK. Calculated (b) final versus initial velocity for the same set of parameters. (c) Corresponding spatial distributions.

however, gravity accelerates the central layer into resonance with the downward propagating molasses beam, causing the two downward propagating layers to merge. For the $t_V=25$ ms time used in Fig. 14, this process is complete. Hence, only two layers are observed with the more (less) intense packets in the Fig. 14 images corresponding to the lower two (uppermost) cube layers.

Comparing the numerically simulated $\delta>0$ spatial distributions with Figs. 14 and 17(a) reveals that theoretically predicted $|d\vec{B}|=0$ lattice spacings are $\sim2\times$ larger than observed. This result occurs due to stray magnetic fields. Here, an independently measured ~100 mG/cm permanent chamber magnetization spatially shifts the effective detuning as the atoms move outward, causing an apparent deceleration and thus reduced lattice spacing. This effect can be seen most clearly by measuring the vertical position of the upward moving cube layer z_T versus t_V. In this case, Eq. (1) predicts that the atoms are accelerated to a velocity v_0 where the radiative force balances gravity. The cloud then moves upward at v_0 and hence, experiences an effective acceleration $g_e=0$. To test for a magnetic field induced nonzero g_e, Fig. 18 shows z_T versus t_V for $s=30$ and $\delta=140$ kHz. The solid line in the figure is a fit to the simple kinematic equation $z_T=z_0+v_0t_V-(g_et_V^2)/2$. Here, v_0 is treated as an initial velocity since for $s=30$ and $\delta=140$ kHz, the atoms are accelerated to v_0 in <2 ms. From the fit, we find $g_e=-0.98(16)$ m/s^2, consistent with a stray gradient $dB_z=100$ mG/cm. Once this gradient is included in numerical calculations of Eq. (1), the
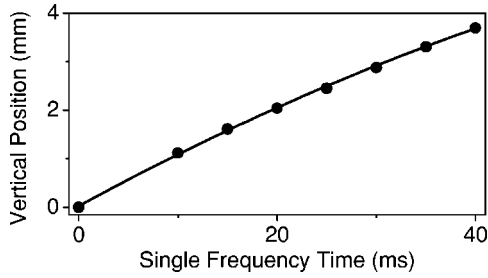
FIG. 18. Measured vertical position of the upward moving layer versus t_V at $\delta=140$ kHz and $s=30$. The solid line is a fit to the model described in the text.

measured and calculated lattice point spacings agree.

Finally, the exceptionally sharp velocity and thus spatial distributions for the upward propagating layer in Fig. 17 imply velocity compression beyond the bunching effects described earlier. In fact, as shown by Fig. 19(a) which depicts the composite gravitational and radiative force for the upward moving atoms, stable cooling occurs around v_0 where the composite force is zero. From Eq. (2), v_0 is given by

$$v_0 = \frac{1}{k}\left(\Delta + \frac{\Gamma}{2}\sqrt{s(R-1)-1}\right), \qquad (13)$$

which depends linearly on Δ and scales approximately as Γ_E. Figure 19(b) shows measured values for v_0 versus δ at $s=10$ and $s=75$, clearly demonstrating the expected linear δ-dependence. To obtain quantitative comparisons with theory, we next perform linear fits to the data and then obtain predicted values for v_0 from numerical calculations that include the 100 mG/cm field gradient discussed above. From the experiment, we find $(\partial v_0/\partial\delta)=644(17)$ μm/(kHz s) at $s=10$ and $634(19)$ μm/(kHz s) at $s=75$. These slopes agree at the 10% level with the predicted values of $(\partial v_0/\partial\delta)=572(5)$ μm/(kHz s) at $s=10$ and $638(20)$ μm/(kHz s) at $s=75$. Moreover, experimentally observed absolute values for v_0 are reproduced by the calculations at the level of 20%, in good agreement with the expected Eq. (13) intensity dependence.
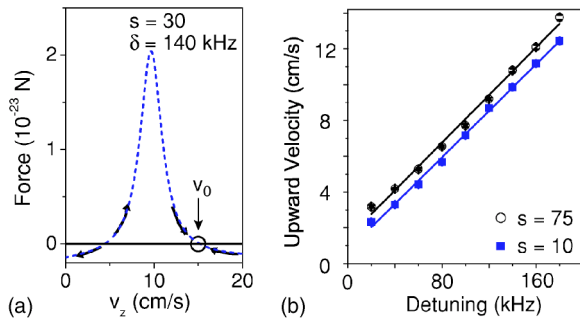

(a)　　　　　　　(b)

FIG. 19. (Color online) $\delta=0$ cooling. (a) Composite gravitational and $\delta>0$ radiative force versus v_z. Arrows show the direction for force induced velocity changes. Stable cooling occurs around a velocity v_0, labeled by the circle, where gravity cancels the radiative force. (b) Measured v_0 versus δ for $s=10$ and $s=75$. Solid lines are linear fits.

The equilibrium temperature of the upward moving layer can be calculated by following the same procedure used to derive Eq. (6). Here, however, we set $\mu dB_z z=0$ in Eq. (2) and perform the Taylor expansion about $v_z=v_0$. The δ-independent effective detuning is then

$$\frac{\Delta - kv_z}{\Gamma} = -\frac{\sqrt{Rs-s'-1}}{2}, \qquad (14)$$

which leads to damping and diffusion coefficients identical to Eqs. (4) and (5), respectively. The expected equilibrium temperature is then given by Eq. (6). Thus, gravity, via the ratio R, again plays an important role in narrow line thermodynamics, in this case enabling $\delta>0$ cooling. Unfortunately, this prediction cannot be accurately verified due to spatial overlap among the horizontal plane packets in the upward moving cube layer. The observed and theoretically predicted sharp vertical spatial distributions in Figs. 17(a) and 17(c), however, strongly suggest that $\delta>0$ cooling is operative in the experiment. Finally, note that although this same cooling mechanism should occur for broad lines where $R \sim 10^5$, v_0 in this case has impractical values on the order of 100 m/s. Moreover equilibrium temperatures are large, at roughly $160\times(\hbar\Gamma_E/2k_B) \sim 200$ mK for the $^1S_0-^1P_1$ transition even at $s=1$.

VII. CONCLUSIONS

In summary, narrow line laser cooling exhibits a wealth of behaviors ranging from novel semiclassical dynamics wherein gravity can play an essential role to quantum mechanically dominated subphoton recoil cooling. In the $\delta<0$ semiclassical case, trap dynamics are set by either hard wall boundaries or a linear restoring force. Qualitative differences between these two situations are reflected in both the atomic motion and the equilibrium thermodynamics. Here, mechanical dynamics range from free-flight in a box potential to damped harmonic oscillation. Accordingly, equilibrium temperatures range from detuning independent values scaled by the power-broadened transition linewidth to detuning dependent minima well below the standard Doppler limit. As the saturation parameter approaches unity, the trap enters a quantum mechanical regime where temperatures fall below the photon recoil limit despite the incoherent trapping beam excitation. For $\delta>0$, the cloud divides into momentum-space crystals containing up to 26 well defined lattice points and the system exhibits $\delta>0$ gravitationally assisted cooling. These surprising $\delta>0$ behaviors, which again occur due to an incoherent process, are theoretically universal features of Doppler limited systems. Observations should therefore be possible, although difficult, with broad line optical molasses. Perhaps a similar $\delta>0$ mechanical evolution also occurs for atoms, such as the more typically employed Alkali metals, that support both Doppler and sub-Doppler cooling.

[1] H. Katori *et al.*, Phys. Rev. Lett. **82**, 1116 (1999).

[2] R. Maruyama *et al.*, Phys. Rev. A **68**, 011403(R) (2003).

[3] X.-Y. Xu *et al.*, Phys. Rev. Lett. **90**, 193002 (2003).

[4] Y. Takasu *et al.*, Phys. Rev. Lett. **91**, 040404 (2003).

[5] T. Ido and H. Katori, Phys. Rev. Lett. **91**, 053001 (2003).

[6] M. Takamoto and H. Katori, Phys. Rev. Lett. **91**, 223001 (2003).

[7] H. Katori *et al.*, Phys. Rev. Lett. **91**, 173005 (2003); T. Mukaiyama *et al.*, *ibid.* **90**, 113002 (2003); T. Ido, Y. Isoya, and H. Katori, Phys. Rev. A **61**, 061403(R) (2000).

[8] E. A. Curtis, C. W. Oates, and L. Hollberg, J. Opt. Soc. Am. B **20**, 977 (2003).

[9] G. Wilpers *et al.*, Phys. Rev. Lett. **89**, 230801 (2002); T. Binnewies *et al.*, *ibid.* **87**, 123002 (2001).

[10] T. H. Loftus *et al.*, Phys. Rev. Lett. **93**, 073003 (2004).

[11] See, for example, H. J. Metcalf and P. van der Straten, *Laser Cooling and Trapping* (Springer-Verlag, New York, 1999), and references therein.

[12] P. D. Lett *et al.*, J. Opt. Soc. Am. B **6**, 2084 (1989).

[13] D. J. Wineland and W. M. Itano, Phys. Rev. A **20**, 1521 (1979).

[14] Y. Castin, H. Wallis, and J. Dalibard, J. Opt. Soc. Am. B **6**, 92046 (1989); H. Wallis and W. Ertmer, *ibid.* **6**, 2211 (1989).

[15] X.-Y. Xu *et al.*, Phys. Rev. A **66**, 011401(R) (2002).

[16] This analogy is not rigorously correct since face-centered-cubic crystals lack the lattice points along corner-connecting lines that are observed in the experiment.

[17] A. Noble and M. Kasevich, Rev. Sci. Instrum. **65**, 9 (1994).

[18] T. E. Barrett *et al.*, Phys. Rev. Lett. **67**, 3483 (1991).

[19] M. Bode *et al.*, Opt. Lett. **22**, 1220 (1997).

[20] A. Derevianko, Phys. Rev. Lett. **87**, 023002 (2001).

[21] M. Yasuda and H. Katori, Phys. Rev. Lett. **92**, 153004 (2004).

[22] T. Loftus *et al.*, Phys. Rev. A **61**, 051401(R) (2000).

[23] T. P. Dinneen *et al.*, Phys. Rev. A **59**, 1216 (1999).

[24] X.-Y. Xu *et al.*, J. Opt. Soc. Am. B **20**, 968 (2003).

[25] T. Loftus, J. R. Bochinski, and T. W. Mossberg, Phys. Rev. A **66**, 013411 (2002).

[26] H. Katori *et al.*, in *Atomic Physics XVII*, edited by E. Arimondo, P. DeNatale, and M. Inguscio, AIP Conf. Proc. No. 551 (AIP, Melville, NY, 2001), p. 382.

[27] T. Loftus *et al.*, in *Laser Spectroscopy: Proceedings of the XVI International Conference*, edited by P. Hannaford, A. Sidorov, H. Bachor, and K. Baldwin (World Scientific, Rivers Edge, NJ, 2004), p. 34.

[28] S. B. Nagel *et al.*, Phys. Rev. A **67**, 011401(R) (2003).

[29] D. P. Hansen, J. R. Mohr, and A. Hemmerich, Phys. Rev. A **67**, 021401(R) (2003).

[30] J. Stuhler *et al.*, Phys. Rev. A **64**, 031405(R) (2001).

[31] A. Derevianko *et al.*, Phys. Rev. Lett. **90**, 063002 (2003).

[32] V. Kokoouline, R. Santra, and C. H. Greene, Phys. Rev. Lett. **90**, 253201 (2003).

[33] R. Santra and C. H. Greene, Phys. Rev. A **67**, 062713 (2003).

[34] A. Avdeenkov and J. L. Bohn, Phys. Rev. A **66**, 052718 (2002).

[35] H. J. Lewandowski *et al.*, J. Low Temp. Phys. **132**, 309 (2003).

[36] R. W. P. Drever *et al.*, Appl. Phys. B: Photophys. Laser Chem. **31**, 97 (1983).

[37] R. J. Jones, I. Thomann, and J. Ye, Phys. Rev. A **69**, 051803(R) (2004).

[38] See J. Ye *et al.*, J. Opt. Soc. Am. B **20**, 1459 (2003) and K. W. Holman *et al.*, Opt. Lett. **29**, 1554 (2004), and references therein.